On the microphysical effects of observed cloud edge charging

Article

It is advisable to refer to the publisher's version if you intend to cite from the work. See Guidance on citing.
Published version at: http://dx.doi.org/10.1002/qj.2554
To link to this article DOI: http://dx.doi.org/10.1002/qj.2554

www.reading.ac.uk/centaur

CentAUR

Central Archive at the University of Reading

Reading's research outputs online

RMetS

Royal Meteorological Society
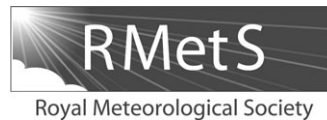
On the microphysical effects of observed cloud edge charging

R. G. Harrison,* K. A. Nicoll and M. H. P. Ambaum

Department of Meteorology, University of Reading, UK

*Correspondence to: R. G. Harrison, Department of Meteorology, University of Reading P.O. Box 243, Earley Gate, Reading, Berks, RG6 6BB, UK. E-mail: r.g.harrison@reading.ac.uk

Liquid layer clouds are abundant globally. Lacking strong convection, they do not become electrified by the usual thunderstorm mechanisms of collisional electrification between hydrometeors of different phases. Instead, the background global circuit current flow in fair weather is largely unaffected by the layer cloud's presence, and, if the layer cloud is extensive horizontally, the vertical fair weather conduction current passes through the cloud. A consequence of the vertical current flow is that, at the cloud–air boundary where there is a conductivity transition and droplets form or evaporate, droplet charging occurs. Charge can affect both droplet evaporation and droplet–droplet collisions. Using new radiosonde instrumentation, the charge observed at layer cloud edges is evaluated for both these microphysical droplet processes. This shows that the charging is more likely to affect collision processes than activation, for small droplets. Enhancing the collection efficiency of small droplets modifies their evolution and propagates through the size distribution to shorten the autoconversion time-scale to rain drops, and the cloud radiative properties. Because the conduction current density is influenced by both external (e.g. solar modulation of high-energy particles) and internal (e.g. El Niño–Southern Oscillation) factors, current flow leading to layer cloud edge charging provides a possible route for expressing solar influences on the climate system and a teleconnection mechanism for communicating internal climate variability.

1.   Introduction

The global atmospheric electric circuit (Rycroft *et al.*, 2000), originally suggested by Wilson (1921, 1929), is a well-established feature of the atmosphere which couples charge separation in disturbed weather regions with current flow in distant fair weather zones. It results from the slight conductivity of atmospheric air caused by cosmic ray ionization and natural radioactivity, combined with the conductive pathways presented by the upper atmosphere and the planetary surface (Aplin *et al.*, 2008). Strong evidence in support of the global circuit was provided by Whipple and Scrase (1936) through the similarity they reported between the diurnal cycle in global thunderstorm area and the surface atmospheric fair weather electric field measured in oceanic air. From measurements made on the multi-ocean cruises of the survey ship *Carnegie*, the diurnal variation in the fair weather atmospheric electric field was found to be both independent of position, and to be aligned with universal time (UTC). This diurnal cycle in atmospheric electricity, with a minimum around 0300 UTC and a maximum around 1900 UTC, is now widely known as the Carnegie curve (Harrison, 2013). It is a characteristic feature of the current flow in the global circuit,

quantitatively demonstrated to be sustained by charge separation in disturbed weather regions (Mach *et al.*, 2011), as depicted in Figure 1(a).

For these purposes, fair weather electrical conditions are those meteorological circumstances in which there is no local charge generation. This necessarily excludes thunderstorm conditions or situations with clouds which are developing their own substantial electric fields. Fair weather conditions do, however, include circumstances when other clouds are present, in particular layer (stratus) clouds, which are globally abundant. When such layer clouds are present and horizontally extensive, the fair weather current must pass through them for charge conservation to apply (Figure 1(b)). This is evident through modelling studies of the global circuit (e.g. Baumgaertner *et al.*, 2014) and has been demonstrated experimentally by comparing measured surface currents in overcast and clear conditions (Nicoll and Harrison, 2009), or through low-level fog layers (Bennett and Harrison, 2009). One consequence is that unipolar charging of droplets occurs in the horizontal cloud boundary regions (Zhou and Tinsley, 2007). This may affect the cloud microphysics at the upper or lower cloud–air boundary (Tinsley, 2000; Tinsley *et al.*, 2000; Rycroft *et al.*, 2012). Evidence suggesting droplet charge
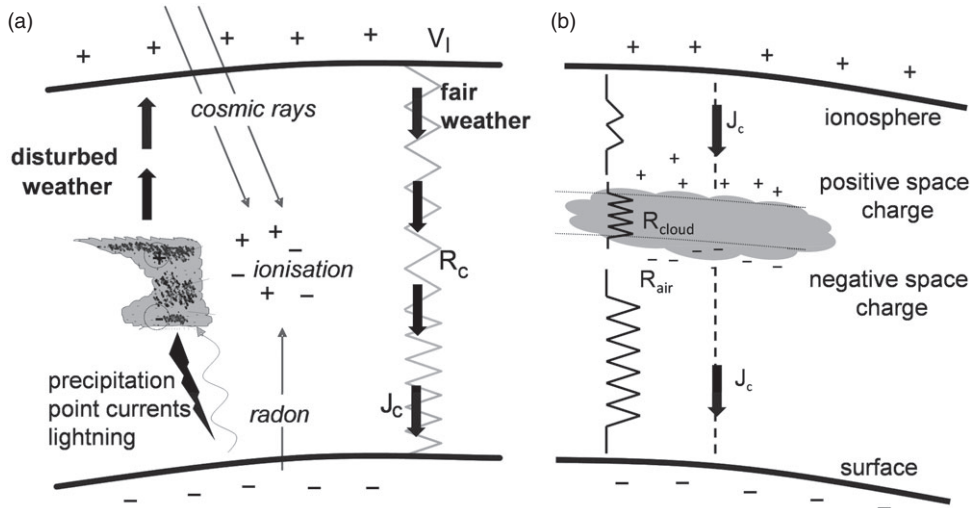
Figure 1. Flow of current in the global atmospheric electric circuit. (a) Charge separation in disturbed weather regions (shower clouds and thunderstorms) leads to current flow between the planetary surface and the conductive regions of the upper atmosphere, which become charged to a potential V_I. A return current (density J_c for a unit area column resistance R_c) flows vertically in fair weather regions where there is no active charge separation. (b) Situation arising when the vertical current density J_c encounters an extensive layer of cloud. The layer of cloud has a resistance, R_{cloud}, greater than that of the cloud-free air, R_{air}.

effects at the lower cloud boundary is apparent in lidar reflection measurements of cloud base made during the polar night, when the usual solar-driven diurnal cycle in cloud base is absent. At both Northern and Southern Hemisphere sites, the diurnal cycle in cloud base height shows, on average, a phase variation similar to the Carnegie curve characteristic of the global atmospheric electric circuit (Figure 2), with comparable amplitude at both sites (Harrison and Ambaum, 2013). Whilst these measurements record a variation in cloud base height, this is primarily determined by the local environmental thermodynamics, hence the lidar measurements are interpreted as demonstrating a change in the droplet properties of the cloud base region in which the optical reflection occurs.

This article considers effects on droplet microphysics which may result from droplet charging at the upper and lower boundaries of layer clouds, where there is coupling to the global circuit current. In section 2, the origin of the droplet charging is considered quantitatively, and in section 3, possible effects of charging on droplet behaviour are compared. Section 4 reports new measurements of cloud edge droplet charging which constrain the effect, with further discussion in section 5.

2. Cloud edge charging

Droplet-laden air has a lower electrical conductivity than cloud-free air; consequently any cloud to clear air boundary will also define a transition in electrical conductivity. The conductivity change occurs because, in droplet (and particle) free air, the cluster ions formed by cosmic rays and natural radioactivity which provide the electrical conductivity of air are only removed by their self-recombination, whereas in cloudy air, the ion concentration becomes considerably reduced by attachment of ions to droplets. The electrical conductivity of air depends on the concentrations of positive and negative ions, with the total conductivity σ_t given by

$$\sigma_t = e(\mu_+ n_+ + \mu_- n_-),\qquad(1)$$

where $\mu_\pm$ represents the mobility of positive or negative ions present, $n_\pm$ the associated bipolar ion number concentrations and e the modulus of the elementary charge. The ion concentration in the presence of droplets or particles is characterised by the ion balance equation (e.g. Harrison and Carslaw, 2003). For a mean ion concentration $n = (n_+ + n_-)/2$, the change of ion concentration with time is given by

$$\frac{dn}{dt} = q_i - \alpha n^2 - (\beta_a N_a + \beta_d N_d)n,\qquad(2)$$

where the first term on the right-hand side q_i is the ion production rate per unit volume, the second term represents the self-recombination rate of ions (with α the ion−ion recombination coefficient), and the third term represents the loss of ions by attachment to aerosol and droplets. This assumes that the aerosol and droplets can be regarded as monodisperse, with N_a the background aerosol number concentration, N_d the droplet number concentration, and β_a and β_d the size-dependent ion−aerosol and ion−droplet attachment coefficients respectively (Gunn, 1954). In clouds ion−ion recombination can be neglected, and ion loss by attachment to droplets dominates over that to aerosol ($\beta_d N_d \gg \beta_a N_a$). Hence in the steady state, the mean ion concentration is

$$n = \frac{q_i}{\beta_d N_d},\qquad(3)$$

and, from Eq. (1), the total conductivity is therefore

$$\sigma_t = \frac{2\mu e q_i}{\beta_d N_d},\qquad(4)$$

where μ is the mean ion mobility. If the limiting form given by Gunn (1954) for the ion−droplet attachment coefficient for uncharged droplets of radius r, is assumed

$$\beta_d = \frac{4\pi kT\mu r}{e},\qquad(5)$$

where k is Boltzmann's constant and T the temperature, Eq. (4) becomes

$$\sigma_t = \frac{q_i e^2}{2\pi kT}\frac{1}{N_d r}.\qquad(6)$$

Some intuition for the conductivity variations can be gained from considering the associated variations in visual range (visibility) as, for both conductivity and visual range, the droplet concentration is the major determining factor (Harrison, 2012). Following Koschmieder's theory, the visual range X_r is given by

$$X_r = \frac{3}{2\pi}\frac{1}{N_d r^2}.\qquad(7)$$

Both X_r and σ are seen to be inversely proportional to droplet concentration N_d.

The vertical conductivity gradient at a cloud edge creates a gradient in the vertical electric field E_z in the same region. Gauss's
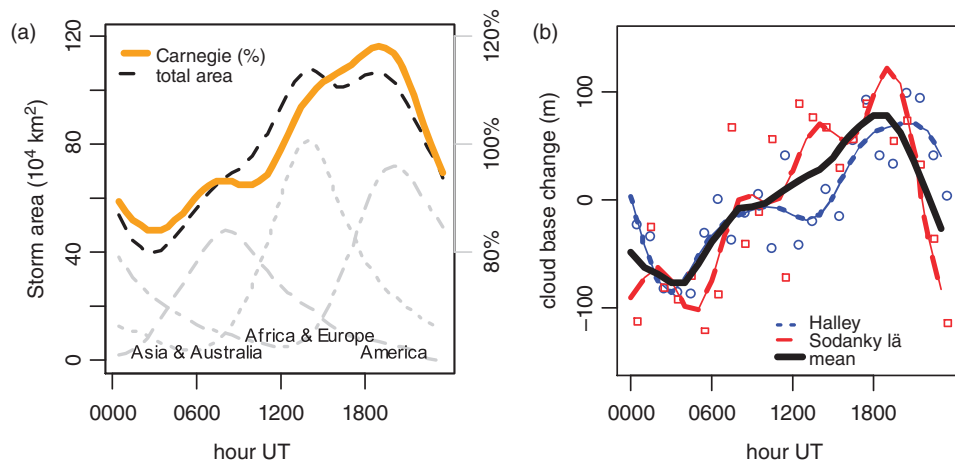
Figure 2. (a) The Carnegie curve of the diurnal cycle in the global atmospheric electric circuit (solid thick line), as a percentage variation of the surface potential gradient using the standard harmonic fit (Harrison, 2013). The dashed lines show the thunderstorm area from Whipple and Scrase (1936), for the three major continental areas of Asia, Africa–Europe, and America (grey dashed lines), and the summed global variation (black dashed line). (b) Averaged diurnal cycle in cloud base height for Halley, Antarctica (blue circles and short dashed line) and Sodankylä, northern Finland (red squares and dashed line), measured during their respective polar nights, with the lines representing harmonic fits to the hourly data. The smoothed mean of the two sites' variations is given by the solid line.

law of electrostatics relates the vertical gradient of electric field dE_z/dz to space charge density ρ by

$$\frac{dE_z}{dz} = -\frac{\rho}{\varepsilon_0}, \tag{8}$$

where ε_0 is the permittivity of free space and z is considered positive upwards. (The presence of aerosols and droplets has negligible effect on ε_0.) Assuming no horizontal divergence of the current in steady-state, and Ohm's law in the vertical dimension,

$$J_c = \sigma_t E_z, \tag{9}$$

the cloud edge charge density can be written in terms of constant vertical current density J_c, as

$$\rho = -\varepsilon_0 J_c \frac{d}{dz}\left(\frac{1}{\sigma_t}\right) = \varepsilon_0 J_c \left(\frac{1}{\sigma_t^2}\right)\frac{d\sigma_t}{dz}. \tag{10}$$

Equation (10) indicates that, for J_c directed downwards, positive charge occurs at the top edge of a horizontal cloud layer where there is an increase of conductivity with increasing height, and negative charge at the bottom edge. Further, the cloud edge charging is proportional to the current flowing through the cloud and the gradient of the conductivity on the cloud edge, i.e. it arises from large-scale changes in the global atmospheric electric circuit and the local meteorological conditions sustaining the cloud. These purely electrostatic considerations have to be seen in the context of the weak dynamical motions occurring within the cloud. The charge structure of layer clouds results from the steady-state between the formation and charging of droplets on the cloud edge, and the transport of the droplets to the bulk of the cloud by turbulent motions.

A practical difficulty in making theoretical charge estimates is that the conductivity in the cloud is a poorly known parameter, and may never have been directly measured (Nicoll, 2012). In the absence of such measurements, by assuming that the conductivity in the cloud is substantially less than that of the clear air, Harrison and Ambaum (2008) showed that the ion–droplet attachment coefficients of Gunn (1954) give an implicit relationship for the droplet charge j as

$$\sinh(2\lambda j) = \frac{J_c}{2Deq_i}. \tag{11}$$

In Eq. (11) $\lambda = \frac{e^2}{8\pi\varepsilon_0 rkT}$ and D is the cloud–air transition region depth, which is, in principle, a more directly observable quantity. Equation (11) also implies that the greatest charging through this mechanism will occur where the ion production rate q_i from surface radioactivity and cosmic rays is at its least, typically at 1–2 km above the surface (Harrison *et al.*, 2014).

3. Consequences of droplet charging

Charging of haze droplets at cloud edges is expected to affect their activation by reducing the minimum supersaturation at which the haze droplets begin to grow (Harrison and Ambaum, 2008). The subsequent evolution of the droplet size distribution may also be affected by electrical effects on collisional interactions (Khain *et al.*, 2004). The relative sensitivities of these processes to droplet charge are now considered quantitatively. An important first aspect is the nature of the electric force between charged droplets, as in general they can become polarised (section 3.1). Section 3.2 considers the effect of charge on droplet formation. Section 3.3 applies the considerations of section 3.1 to calculating droplet–droplet collision efficiency in the charged case and the effects of the enhanced collision efficiency on evolution of the droplet size distribution.

3.1. Inter-droplet electric forces

Unlike the well-known Coulomb force between two point charges, the electric force between two conducting spheres carrying the same polarity of charge can be attractive when the two spheres are close together. This occurs because conducting spheres (or droplets) are polarisable, and an image charge of opposite polarity can be induced in one sphere by the charge on the other. For the case of two water droplets, polarised regions of opposite charges generate an attractive force, and consequently the droplet–droplet interaction can be substantially different to that between neutral droplets.

In the simplest case of two point charges q_1 and q_2, the Coulomb force F_C between centres of the point charges separated by a distance x has a magnitude

$$F_C = \frac{1}{4\pi\varepsilon_0}\frac{q_1 q_2}{x^2}, \tag{12}$$

where ε_0 is the permittivity of free space. Equation (12) leads to a repulsive force if the two point charges have the same polarities. However, when two charged conducting spheres approach each other, polarisation leads to an infinite set of image charges being induced by each sphere in the other. The image charges are particularly important when the spheres are close, and a summation of all the terms concerned with each image–image interaction is required to find the net force as discussed in standard electrostatics texts (e.g. Smythe, 1950). As an illustration, for two conducting spheres having the same radius r, an approximation to the total electric force F_E between them was given by
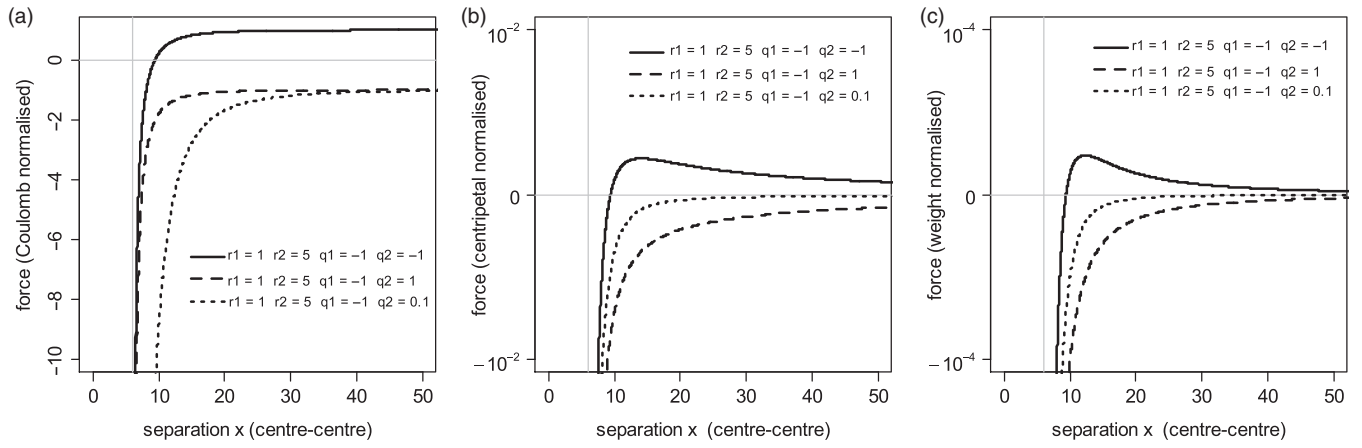
Figure 3. Electric force between a droplet of radius r_1 and drop of radius r_2 ($r_2 > r_1$) carrying different charges (q_1 and q_2), against separation distance x. In both cases the separation (x-axis) between the two drops given is normalized by the small drop radius r_1, and negative forces are attractive. The force has been normalized in (a) by the Coulomb force between the two drops and in (b) by $m_1 v^2 / x$, where v is the difference in the terminal fall speeds, m_1 the mass of the smaller droplet and x the separation and (c) by the weight of the smaller drop. ((b) amounts to normalisation by the centripetal acceleration which would be experienced if the smaller droplet were to execute a circular orbit around the larger drop.)

Russell (1922) as

$$
\begin{aligned}
F_{\mathrm{E}} \approx{} & \frac{q_1 q_2}{4\pi\varepsilon_0 x^2}\left(1 + \frac{14}{y^6} + \frac{54}{y^8}\cdots\right) \\
& - \frac{q_1^2 + q_2^2}{4\pi\varepsilon_0 x^2}\left(\frac{2}{y^3} + \frac{3}{y^5} + \frac{4}{y^7} + \frac{25}{y^3(y^2-1)^3}\right. \\
& \left. + \frac{75}{y^5(y^2-1)^3}\cdots\right),
\end{aligned}
\tag{13}
$$

where $y = x/r$, for x the separation between the spheres' centres. For large y, the second term contributes little, but as the spheres move closer and y decreases, the contribution of the second term increases. Importantly, this is independent of the polarities of q_1 and q_2. For charged droplets, even if they have the same polarity, the inter-droplet force will become attractive at small separations, except in one hypothetical case, when both droplets have charges which would generate precisely equal potentials on contact (Thomson, 1853). A consequence of the limited number of terms in Russell's approximation is that it considerably underestimates the electric force when the droplets are close. It is possible to make other approximations in some regimes of varying effectiveness (e.g. Khain *et al.*, 2004; Fletcher, 2014; Tinsley and Zhou, 2014), but, to accurately evaluate the force between droplets of arbitrary radii and charges, a full summation of all the interaction terms is needed (Davis, 1964; Lekner, 2012).

Figure 3 shows the inter-droplet force calculated using the full summation for a variety of radii (for clarity, when the sizes differ, 'drop' is used to refer to the larger of the two droplets), with charge loadings quantified in terms of elementary charges. Three situations are evaluated for equal and opposite charges on both drop and droplet ($q_1 = -1$ and $q_2 = +1$), equal charges on both ($q_1 = 1$ and $q_2 = +1$) and a charged droplet along side a negligibly charged drop ($q_1 = 1$ and $q_2 = 0.1$). In (a) the force has been normalised by the equivalent Coulomb force between point charges, in (b) by the horizontal force between two drops falling vertically at terminal velocity and in (c) by the (smaller) droplet's weight. (These situations are summarised schematically in the appendix, in Figure A1(a).) In each case the magnitude of the force asymptotes to the value of the Coulomb force, and, as the droplet size increases, the range over which the attraction occurs diminishes. When the drop charge is small, the Coulomb force is also small and hence the normalisation in Figure 3(a) leads to a substantial relative electric force. The normalisations in Figure 3(b,c) illustrate that, whilst the long-range force is up to a few per cent of that associated with the inter-droplet force, it is small in terms of the droplet weight. It is therefore not expected to influence the droplet's trajectory. However, on close approach, the image

forces become large and attractive, even when only the droplet is charged, substantially increasing the likelihood of the drop and droplet sticking. This amounts to the collision cross-section of the collecting drop being increased, which the calculations in Figure 3 suggest can be equivalent to an increase in its radius by about 10–20%. (This is considered further in section 3.3.)

3.2. Condensation and evaporation

Charging of a water drop modifies a droplet's potential, and therefore the Gibbs free energy associated with its formation by condensation (Mason, 1971; Ambaum, 2010). For a drop of radius r, this brings an associated change in free energy ΔG of

$$
\Delta G = -\frac{4}{3}\pi r^3 \rho_{\mathrm{L}}\frac{N_{\mathrm{A}}}{M_{\mathrm{r}}}kT\ln S + \frac{q^2}{8\pi\varepsilon_0}\left(\frac{1}{r}\right),
\tag{14}
$$

where N_{A} is Avogadro's number, M_{r} is the relative molecular mass, ρ_{L} is the density, and q is the charge on the condensation nucleus. S is the saturation ratio of the moist environment of the drop which includes the surface tension (Kelvin) effect, as well as the dissolved salt (Raoult) effect. The saturation ratio required for a droplet of radius r to form is conventionally found (Mason, 1971) by solving for S when $\frac{\mathrm{d}(\Delta G)}{\mathrm{d}r} = 0$. Including the additional term from Eq. (14), this gives

$$
S(r) = \frac{\exp\left(\frac{r_K}{r}\right)\exp\left(-\frac{r_{\mathrm{K}}r_{\mathrm{R}}^3}{r^4}\right)}{\left(1 + \frac{b}{r^3}\right)}.
\tag{15}
$$

Here, r_K is the Kelvin radius $r_{\mathrm{K}} = \frac{2\sigma_{\mathrm{L}}}{\rho_{\mathrm{L}} R_{\mathrm{v}} T}$ and b the Raoult (dissolved salt) term $b = \frac{3 i_{\mathrm{V}} M_{\mathrm{r}} m}{4\pi\rho_{\mathrm{L}} M_{\mathrm{S}}}$, where R_{v} is the gas constant for water vapour, σ_L is the surface tension, T the temperature, i_{V} the van't Hoff factor, M_{S} the relative molecular mass of the salt and m the dissolved mass of salt (Ambaum, 2010). r_{R} is the Rayleigh radius, which is the radius of a charged drop at which the internal electric force balances the surface tension force (and below which radius it will electrically explode.) The Rayleigh radius is given by

$$
r_{\mathrm{R}} = \left(\frac{q^2}{64\pi^2\varepsilon_0\sigma_{\mathrm{L}}}\right)^{1/3}.
\tag{16}
$$

Equation (15) allows evaluation of the saturation ratio required to form a droplet of a particular radius, and, through the salt and Rayleigh radius terms, the relative effect of dissolved salt and charging can be compared. As a consequence of either dissolved salt or charging, the vapour pressure over the droplet
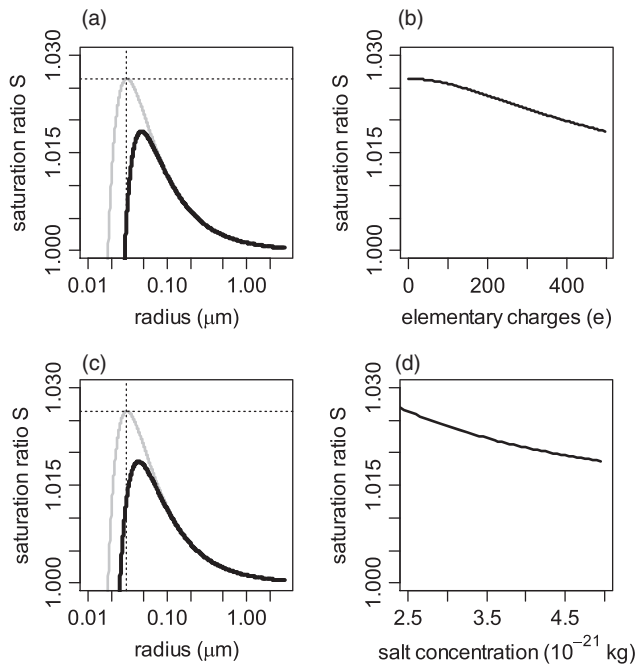
Figure 4. Variation of critical supersaturation with droplet radius, as charge and dissolved salt concentrations are varied. (a) Critical supersaturation versus radius for a neutral droplet with 2.5×10^{-21} kg dissolved salt (grey line), and the same purity droplet carrying 500 elementary charges (black line). (b) Variation of critical supersaturation with charge for a droplet with 2.5×10^{-21} kg dissolved salt. (c) Critical supersaturation versus radius for a neutral droplet with 2.5×10^{-21} kg dissolved salt (grey line), and a neutral droplet with 5×10^{-21} kg dissolved salt (black line). (d) Variation of critical supersaturation with dissolved salt concentration for a neutral droplet. Parameters assumed: surface tension of water $\sigma_L = 7.5 \times 10^{-2}$ N m^{-1}, density of water $\rho_L = 10^3$ kg m^{-3}, relative molecular mass of NaCl $M_S = 0.040$ kg mol^{-1}, air temperature $T = 273$ K, van't Hoff factor $i_V = 2$.

falls and the critical supersaturation is reduced and the associated critical radius increased. (This is because evaporation is inhibited, because, with decreasing radius, the electrical potential energy is increased.) Figure 4 shows this comparison, by plotting the critical supersaturation ratio against the droplet radius as (Figure 4(a,b)) the charge is varied, and (Figure 4(c,d)) as the dissolved salt concentration is varied. For the charge effect to become apparent in Figure 4(a,b), the dissolved salt concentration has to be very low (Harrison and Ambaum, 2008). Only a small amount of dissolved salt (5×10^{-21} kg) is needed to provide a comparable reduction in critical supersaturation with that caused by 500e elementary charges and therefore the effect of impurities is expected to dominate. Numerically, the change from 2.5×10^{-21} to 5.0×10^{-21} kg is equivalent to a change from about 26 000 to 51 000 dissolved salt molecules, hence the effect of a single elementary charge on the vapour pressure is equivalent to about 100 salt molecules.

3.3. Collisions between charged droplets

Capture of one droplet by another drop or droplet is central to the development of the droplet size distribution within liquid water clouds. The effect on this process from charging of either or both droplets is usually found by considering the steady-state flow carrying a smaller droplet around a larger drop, the latter considered stationary. From calculations of the trajectories, the collision efficiency is defined as the ratio of the cross-sectional area described by the droplet's launch position to the geometrical collision cross-section of the larger drop, when a grazing trajectory occurs (Pruppacher and Klett, 1998). This is illustrated in Figure A1(b). Such an approach has been adopted by many authors (e.g. Beard and Grover, 1974), and extended to include electrical interactions (e.g. Schlamp *et al.*, 1975; Klimin *et al.*, 1994; Tinsley *et al.*, 2000; Tripathi and Harrison, 2002; Khain *et al.*, 2004).
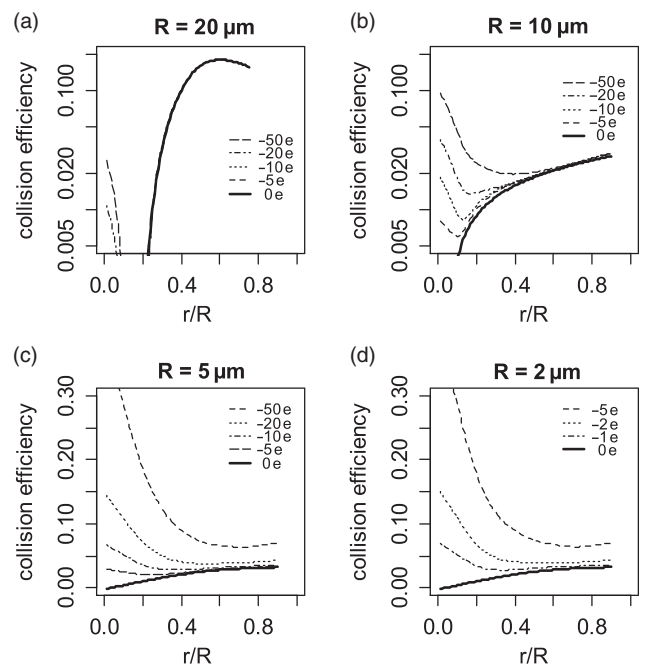
Figure 5. Collision efficiency calculated between a droplet of radius r and a collecting drop of (a) radius $R = 20\,\mu$m and (b) radius $R = 10\,\mu$m, for a range of identical charges on both drop and droplet. (c, d) Calculations for a smaller neutral droplet, with the charge solely on the larger drop of radii $R = 5\,\mu$m and radius $R = 2\,\mu$m respectively. All calculations assume a background electric field of magnitude 100 V m^{-1}.

Collision efficiency calculations for charged drop interactions likely in semi-fair-weather conditions are given in Figure 5, using the model of Klimin *et al.* (1994). This uses the conventional approach of establishing a flow field for a droplet moving around a collecting drop, by a numerical solution to the Navier–Stokes equation. The force between the drop and droplet is calculated using the full summation including image attractions, from Davis (1964). The droplet's trajectory around the collecting drop is found by integrating simultaneous first-order differential equations in time for the velocity and displacement, using drag coefficients based on the Reynolds number. By repeating the calculations with different displacements y_c from the axis where the droplet begins its trajectory (Figure A1(b)), the critical value of y_c giving the grazing trajectory is obtained, allowing the collision efficiency to be determined. As can be seen from Figure 5(a), the collision efficiency associated with a 20 μm radius collecting drop only begins to become appreciable as the collected droplet becomes larger than about 5 μm, as the geometrical collision cross-section also increases. For smaller sizes, the collision efficiency becomes negligible. Similarly, for collecting drops of (Figure 5(b)) 10 μm, (c) 5 μm and (d) 2 μm, the collision efficiency for neutral interactions is small, because of the negligible geometric collision cross-sections. When charged, the collision efficiency of the smaller drops increases considerably, due to the image force attraction at close approach. The calculations show that, in the case of the 10 μm collecting drop, charges of $\sim$50e are sufficient to provide collision efficiencies comparable with that of a neutral 20 μm collecting drop, and, for 5 μm drops, even modest charging of 10e can increase the collision efficiency by an order of magnitude. For small droplets of 2 μm radius, soon after their formation by condensation, the collision efficiency is much more substantially increased. Whilst there will be limitations in these calculations, in particular from inaccuracies in the representation of the flow field, expectations from the force calculations of Figure 3 are nevertheless confirmed, in that the electric force effects are greatest for the smallest drops. The attractive force at close approach is consistent with an electrical enhancement of the geometrical collision cross-section, leading to an increase in the collection of charged small drops compared with that for neutral small drops. Whether or not the collision results in collection
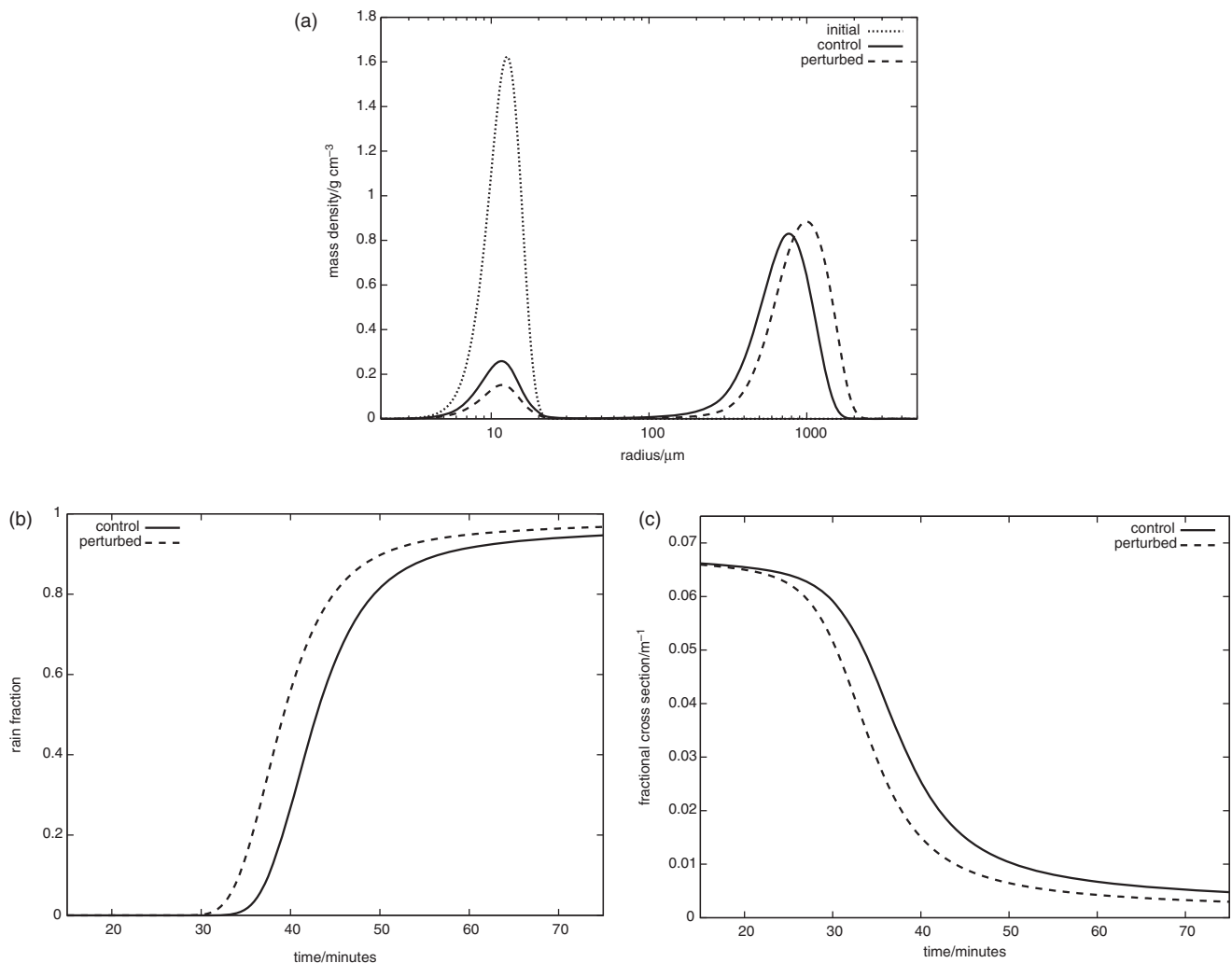
Figure 6. (a) Evolution of the droplet size spectrum from an initial distribution of cloud droplets (dotted line), for a control situation in which the droplets are free to collide and grow (solid line), and a perturbed situation (dashed line) in which the droplets having radii less than 10 µm are given an enhanced collection efficiency, equivalent to a 20% increase in the collecting drop's radius. Variation in (b) the conversion time of cloud droplets to rain drops (drops with radii greater than 0.5 mm), and (c) the fraction of the cross-section occupied by droplets, both found for the size distribution in (a). In each plot the control case (solid line) is compared with a perturbed case (dashed line) when there is an enhanced collection efficiency of droplets with radii less than 10 µm.

of the droplet by the drop depends on the detail of the collision and surface properties, but the implication of these calculations is that, rather than strongly modifying the trajectory, charging will increase the probability of collection following the drop–droplet collision.

The effect of such enhanced collection on the evolution of a cloud droplet distribution is now briefly considered using the cloud microphysics model of Bott (2000). From an initial assumed droplet distribution, this model allows calculation of the droplet distribution at subsequent times, as a result of collisions between the droplets. This methodology is employed to generate a control run, which uses a standard Hall kernel for the collisional interactions to evolve the droplet population, with a perturbed run where the effective geometric size of the larger collecting drop is increased by a percentage which depends on the size of the colliding drop, to represent the increased collision efficiency resulting from charging. This increase reaches a maximum of 20% for collisions with the smallest drops, while it reduces rapidly for collisions with drops larger than 10 µm. In other words, only those collisions involving the very smallest drops (smaller than 10 µm) are enhanced and all the other collisions are unaffected. Figure 6(a) shows the initial droplet population and the droplet population after 45 min, for both the control and perturbed runs. This can also be interpreted in terms of the time evolution of the droplet spectrum, which has effects on the cloud lifetime and its radiative properties. Figure 6(b) indicates, for both runs, what fraction of drops (in terms of mass) exceeds 0.5 mm in radius, as a function of time. The perturbed

run indicates that the autoconversion rate for charged drops may well be substantially larger than that for neutral drops; the corresponding time-scale over which small drops are converted to rain is substantially shorter. Figure 6(c) shows evolution of the fraction of the cross-sectional area occupied by droplets, calculated from the successive droplet size distributions. It can be seen that, for the charge-perturbed case which leads to more of the smaller drops being removed than in the control case, the fractional cross-section due to droplets is reduced, which would modify the radiative properties of the cloud.

4. Cloud charge measurements

Despite the theoretical expectations of electrical effects on cloud microphysical processes, few *in situ* measurements of charges in layer clouds exist, making it difficult to determine which of the droplet charging mechanisms discussed in section 3 is likely to dominate. Determining the thickness of the cloud-to-air transition region provides an approximate method for estimating the droplet charge (Eq. (11)), but even this quantity cannot be obtained at high resolution by conventional meteorological balloon soundings of thermodynamic quantities derived from temperature and relative humidity. To determine the typical charges on droplets in stratiform clouds, combined *in situ* measurements of charge and the cloud boundary dimensions are required. New instrumentation developed to exploit standard meteorological radiosondes as the carrying platform (Harrison *et al.*, 2012) is well-suited to this task, as radiosondes offer the
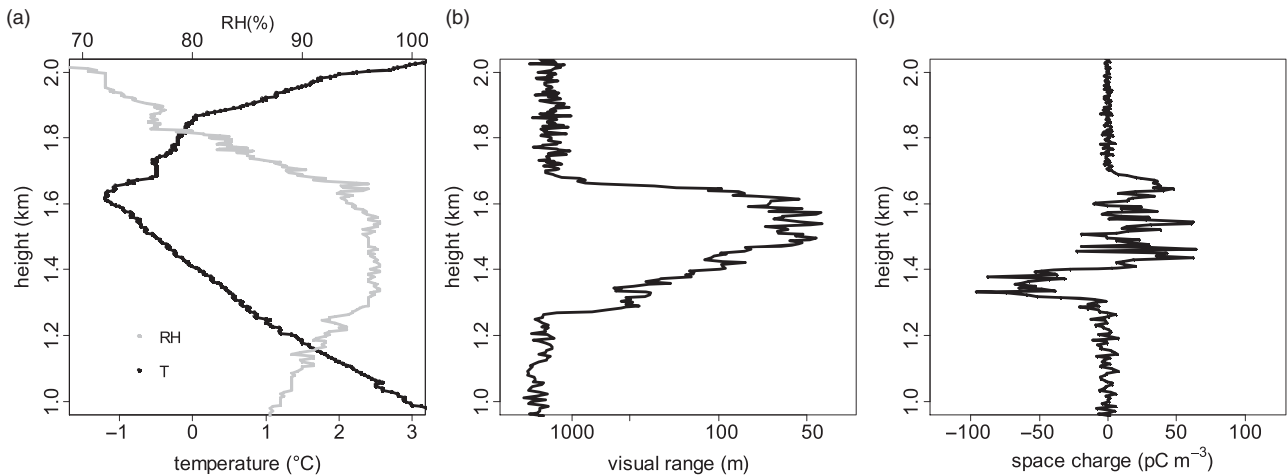
Figure 7. Vertical profiles from a balloon ascent through a layer of stratiform cloud over Reading, UK. (a) Temperature (T, black) and relative humidity (RH, grey) measured by the meteorological radiosonde, with (b) visual range measured by the cloud visibility sensor and (c) space charge density measured by the balloon-borne charge sensor. Part figures (a) and (b) are adapted from Harrison and Nicoll (2014).

capability to respond rapidly to suitable cloud conditions, and the ability to access cloud layers at a range of altitudes and provide thermodynamic and position information (e.g. Harrison, 2015).

4.1. Instrumentation

Two new instruments have been added to the standard Vaisala RS92 radiosonde package to provide the high spatial resolution detection of cloud and simultaneous sensing of the local electrical properties required. Optical detection of cloud provides an enhanced time response over thermodynamic (humidity) based measurements (Nicoll and Harrison, 2012), and therefore, for a vertically moving balloon, improves the determination of the extent of the cloud boundary. The optical detection is achieved using a cloud visibility sensor employing an open path system of a high-brightness light-emitting diode at 590 nm and a photodiode receiver for the backscattered light (Harrison and Nicoll, 2014). This provides the visible range X_r, which, as evident from Eqs (6) and (7), will show a marked change at the cloud boundary where the conductivity transition also occurs. (X_r is typically $5-500$ m inside cloud and very much greater outside cloud.) Simultaneous measurements of the in-cloud charge are made using a small electrode and electrometer arrangement, which responds to displacement currents caused by motion through regions of space charge (Nicoll, 2013). The sensor capacitance was determined in a separate experiment by exposing it (in a fixed position near the surface) within a dynamic fog layer, and the displacement currents induced by charges present in the fog compared with simultaneous atmospheric electric field measurements.

4.2. Cloud measurements and charge estimates

Figure 7 shows measurements from the combined cloud and charge sensor instrument package carried on a radiosonde launched from the Reading University Atmospheric Observatory, through a persistent stratiform cloud. (Both sensors were mounted on the radiosonde itself.) This cloud layer had properties very typical of stratiform cloud at this location, and Figure 7(a) shows the thermodynamic measurements of temperature and relative humidity as measured by the radiosonde during the ascent of the instrumentation through the cloud layer. Using just the thermodynamic data, the lapse rate and temperature inversion suggest a cloud top at about 1.6 km altitude and the relative humidity indicates cloud base at about 1.2 km. From these measurements alone, the existence of the cloud region is clear, but the dimensions of the boundary transition regions defining the electrical properties are only poorly determined. The results

from the optical detection method are shown in Figure 7(b). This shows the cloud boundary region much more distinctly, and the cloud-to-air transition is obtained at a vertical resolution of about 5 m from the sampling rate of 1 Hz and ascent rate of 5 m s^{-1}. Figure 7(c) shows the associated variation in charge density, with up to -100 pC m^{-3} of charge determined in the cloud base and 65 pC m^{-3} near cloud top. The polarity of the charged regions, with negative charge in the cloud base and positive charge at cloud top, is consistent with the theoretical expectations of section 2, and modelled by Zhou and Tinsley (2007).

From Eq. (10), for steady J_c, the cloud boundary charge is proportional to the vertical conductivity gradient at the cloud edge. As discussed earlier, this is closely related to the associated vertical gradient in visual range determined by the optical sensor. Accordingly, Figure 8 shows the detail of the visual range changes at (a) the cloud top and (c) the cloud base regions for the cloud layer of Figure 7. It is evident that the vertical gradient in the visibility (related to the vertical gradient in conductivity through Eqs (6) and (7)) differs between the top and base of the cloud, with the transition from clear to cloudy air sharper in the cloud top region (extending over 70 m) than in the base (extending over 140 m). This is consistent with the thermodynamic profile of the cloud, with a sharp temperature inversion at the cloud top (shown in Figure 8(a)). Associated distributions of the measured space charge for the top and bottom regions are shown in Figure 8(b,d) respectively, which again demonstrates asymmetry between the cloud top (median 33 pC m^{-3}, range 8 to 48 pC m^{-3}) and the cloud base (median -38 pC m^{-3}, range -96 to -6 pC m^{-3}). As cloud droplet number concentrations inside stratocumulus cloud are typically ~100 cm^{-3}, and only show modest variations from this (Miles *et al.*, 2000), an estimate of the droplet charge can be obtained. If the charge density ρ detected is assumed to be partitioned equally across N_d cloud droplets per unit volume, the mean number of elementary charges per droplet j is given by
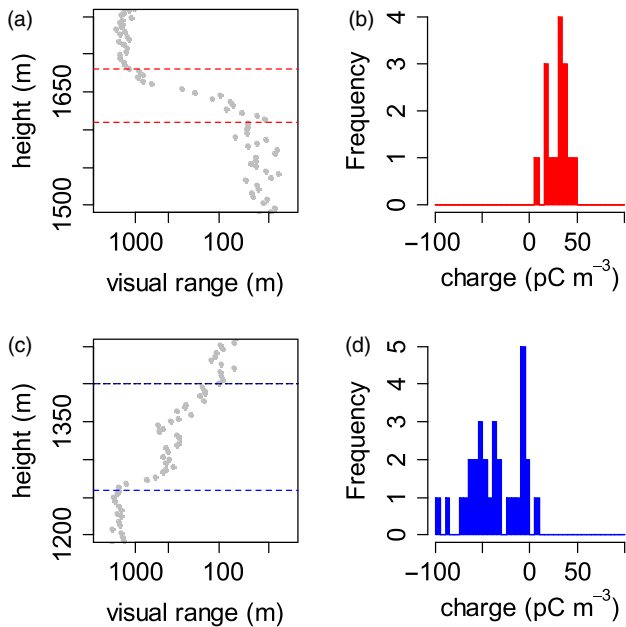
$$j = \frac{\rho}{N_d e}. \tag{17}$$

On this basis, the equivalent mean charge per droplet at cloud top can be estimated as $+5e$ (ranging from $+1$ to $+8e$) and, at the rather less well-defined cloud base, $-6e$ (ranging from -1 to $-16e$).

5. Discussion

Quantitatively, the change in visual range X_r with height can be seen from Eq. (7) to be

$$\frac{dX_r}{dz} = -X_r \left(\frac{2}{r} \frac{dr}{dz} + \frac{1}{N_d} \frac{dN_d}{dz} \right), \tag{18}$$

ⓒ 2015 The Authors. *Quarterly Journal of the Royal Meteorological Society* published by John Wiley & Sons Ltd on behalf of the Royal Meteorological Society.

Q. J. R. Meteorol. Soc. (2015)

Figure 8. Visual range variation in (a) the top and (c) the base of the cloud layer of Figure 7. Measured space charge density for (b) cloud top and (d) cloud base, respectively.

i.e. it is related to both the change in droplet size r and concentration N_d. The partitioning of the changes in these two quantities with height (and therefore the two terms in Eq. (18)) will differ at cloud base and cloud top. At cloud base, the droplets grow initially in updraughts by condensation, causing r and N_d to increase. At cloud top, spontaneous evaporation into the dry air are likely to cause the $\frac{dN_d}{dz}$ term to dominate. However, both the variations in r and N_d lead to changes in the conductivity, and hence vertical changes observed in X_r can be expected to be associated with vertical changes in σ_t. The visual range sensor can therefore be used to estimate the cloud edge charge by the cloud–air transition distance, Eq. (11), for comparison with those from Eq. (17).

Figure 9(a) shows the calculated drop charge for a range of values of vertical cloud–air transition distance D, and ion production rate q_i. At the cloud altitude of $\sim$1500 m, q_i will be determined by contributions from radon isotopes and, to a lesser extent, cosmic rays. Recent measurements at the same site (Harrison *et al.*, 2014) show that the cosmic ray contribution at this altitude is about 2 ion pairs cm^{-3} s^{-1}, although the radon contribution is not known. Even so, it is likely that the ion production rate is much less than the conventionally assumed surface value of 10 ion pairs cm^{-3} s^{-1} (Chalmers, 1967). The effect of reducing q_i is to reduce the air conductivity, and, as Eq. (9) shows, accordingly increase the cloud droplet charge. Hence, for the altitudes typical of low clouds, where the surface radon effect has diminished (or is absent over the oceans) and the cosmic ray contribution remains considerably less than its maximum value at about 20 km, the droplet charging effect is likely to be at its greatest. It is also conceivable that the local ion production rate could fluctuate in some circumstances, such as through radon release associated with earthquakes, or from the artificial introduction of radioactivity or corona ions.

Figure 8 shows that D for the cloud considered is typically $50-100$ m, although there are other changes observed on shorter length scales which may lead to stronger gradients locally. From Figure 9(a), these transition distances would lead to about $2-5$ elementary charges per droplet. Figure 9(b) shows the variation in measured charge within the cloud, drawn alongside Figure 8(a) for comparison. The measured and calculated charges are reasonably consistent for the conservative choices made about the electrical and droplet parameters. However, it is clear that the lower cloud charge is not coincident with the lower cloud

boundary as determined by the visual range sensor, whereas the cloud top is more closely aligned with the charged region. The active measurement regions for both the charge and visual range sensors are likely to be within a few metres of the radiosonde, hence the $\sim$50 m displacement between the observed cloud base and charged droplet zone may be a real phenomenon. The wavelength used for the visual range detector (590 nm) suggests that its optical response will include micron-sized droplets soon after their formation. Some further droplet growth in the cloud updraught may therefore be needed for charge to be detected. A typical charging time-scale is $\sim 1/(\beta_d N_d)$ (Harrison and Carslaw, 2003), which, from Eq. (5), is about 1 min for 5 μm droplets. Hence, for typical updraught speeds $\sim$1 m s^{-1}, this time-scale is consistent with the 50 m displacement between the cloud base and charged region. At the cloud top, much larger drops will be present, which evaporate by the entrainment of drier air above the cloud. In comparison, the clear air to cloud base transition is therefore less distinct; this provides further evidence of asymmetry between the electrification at cloud base and cloud top.

As discussed in section 3, there are several physical consequences associated with the charging of cloud droplets. In an extreme case, perhaps at the cloud top, loss of drops may be enhanced through charging, as, during evaporation, the Rayleigh stability limit may be reached, causing the droplet to spontaneously fragment. More generally, however, the effect of varying the charge state of small droplets, as shown from Figure 6, is that the associated modification of collection efficiencies leads to changes in the droplet size distribution, and the rate of evolution of cloud droplets to raindrop sizes, with possible further implications for cloud lifetime. The detailed cloud environment will modify these changes further, for example because of turbulence and updraught effects. However, these electrically induced changes in droplet size distribution may sometimes be observable in remotely sensed parameters of the cloud from the ground for cloud base or by satellite for cloud top, for example the reflection of short wavelength radiation or the long-wave emissivity. The calculations of Figure 6(c) suggest that, in the charge-perturbed case, a ceilometer beam would need to travel further into a cloud before being reflected, and that the long-wave emission from the top of the cloud would occur from lower down in the cloud. It is therefore clearly possible that the cloud base changes demonstrated in Figure 2 (in which increased charging is associated with a ceilometer return further into the cloud) could be related to the electrical modification of the droplet size distribution in the cloud base. Furthermore, previously reported effects on cloud top temperature (Marsh and Svensmark, 2000; Takahashi *et al.*, 2010) or precipitation (e.g. Neff *et al.*, 2001) associated with solar changes may be the expression of cloud droplet changes associated with the atmospheric electrical environment.

6. Conclusions

These new combined measurements of the cloud edge region in a stratiform cloud demonstrate the global circuit driven electrification expected from theory at all horizontal cloud boundaries, to a greater or lesser extent depending on the vertical cloud boundary gradient. Layer cloud horizontal edges are highly dynamic regions where droplet formation and evaporation occurs continuously, and therefore some of the cloud droplets which become charged will also find their way into the interior of the cloud, as apparent from Figure 7. It is also clear that the cloud edge charging differs between the cloud top and bottom, because of the difference in the thermodynamic structures determining droplet activation at the cloud base and evaporation at the cloud top. In terms of the amount of charge concerned with the droplets at the cloud edge, the estimates of section 4 suggest that, given the context presented by the discussion in section 3, the droplet
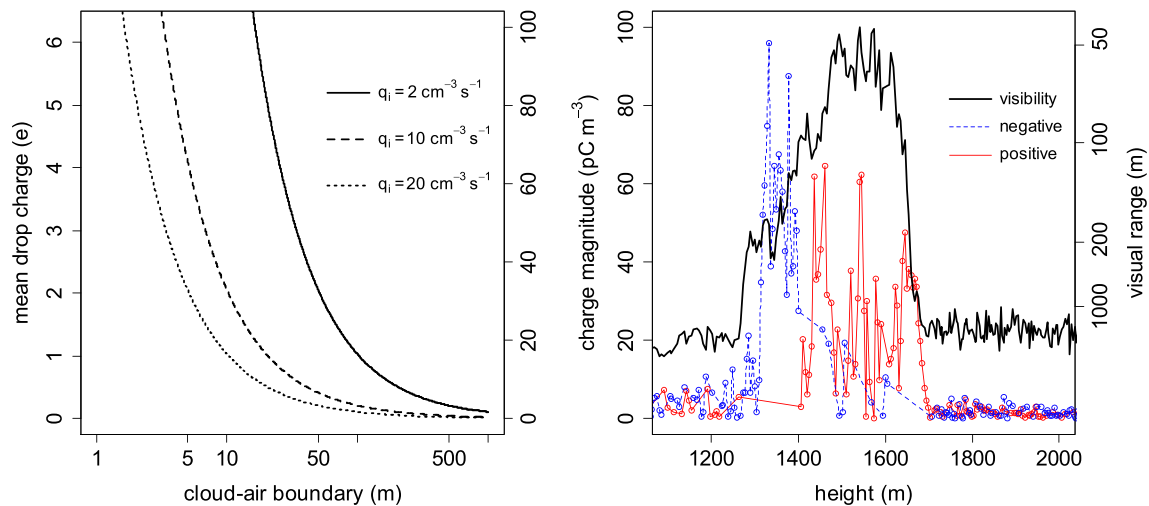
Figure 9. (a) Calculation of mean drop charge with cloud–air boundary thickness for a range of ion production rates q_i and 10 μm radius drops, with (right-hand axis) the equivalent charge density for $N_d = 100$ drops cm^{-3}. Assumptions: conduction current density $J_c = 2$ pA m^{-2}, air temperature 273 K. (b) Positive (red line) and negative (blue line) charge density plotted with height, with the visual range determination (black line) also shown (right-hand axis).

collisional processes are much more likely to be affected than those of activation. The effect of charging in enhancing collection efficiency can, as illustrated by Figure 6, be simply included for cloud modelling purposes by modifying the geometry of the droplets considered.

Although more experiments are planned, the unexceptional thermodynamic nature of the observed cloud indicates that many stratiform clouds will contain charged droplets from the edge charging process. This means that, through the vertical electric current density, coupling can occur between the global circuit and cloud properties, and therefore that those factors modulating the global circuit can also, in principle, couple into clouds. Of these factors, those probably of most interest are of solar origin, which can modulate atmospheric electrical parameters on both solar cycle (Harrison and Usoskin, 2010) and hourly (Nicoll and Harrison, 2014) time-scales. However there is also evidence suggesting the global circuit responds to internal climate variability (e.g. Sátori and Zieger, 1999; Harrison *et al.*, 2011), and therefore there is the possibility of long-range electrical coupling of this variability to the properties of extensive layer clouds.

Appendix

Electrical interactions between drops

The effect of the electric force between polarisable droplets, at close approach, is strongly influenced by the image force attraction. Calculations require a summation of the infinite set of image charges induced between the interacting droplets. The electric force can be compared with the long-range electrical force which would occur between two point charges, the weight of one of the droplets, or the force implied by the centripetal acceleration between the drops. These are shown schematically in Figure A1(a). Figure A1(b) depicts the flow of a smaller droplet around a larger collecting drop, to illustrate the geometrical considerations on which the collision efficiency is defined.
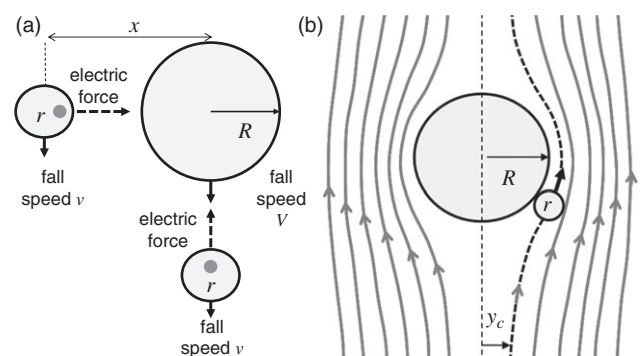
Figure A1. (a) Possible droplet–drop interactions by electric forces, firstly for small droplets (radius r and fall speed v) horizontally adjacent to a large charged drop (radius R and fall speed V), and, secondly, droplets vertically beneath a charged drop. In the first case, the electric force can be compared with $\frac{m(v-V)^2}{x}$ where m is the mass of the droplet and x the droplet–drop separation, and in the second case, with the weight of the droplet, mg. (b) Collision of a droplet passing along the streamlines around a drop. The collision efficiency is defined as $\frac{y_c^2}{(r+R)^2}$, where y_c is the maximum off-axis displacement from which a collision results.

References

Ambaum MHP. 2010. *Thermal Physics of the Atmosphere.* Wiley-Blackwell: Chichester, UK.

Aplin KL, Harrison RG, Rycroft MJ. 2008. Investigating Earth's atmospheric electricity: A role model for planetary studies. *Space Sci. Rev.* **137**: 11–27, doi: 10.1007/s11214-008-9372-x.

Baumgaertner AJG, Lucas GM, Thayer JP, Mallios SA. 2014. On the role of clouds in the fair weather part of the global electric circuit. *Atmos. Chem. Phys.* **14**: 8599–8610, doi: 10.5194/acp-14-8599-2014.

Beard KV, Grover SN. 1974. Numerical collision efficiencies for small raindrops colliding with micron size particles. *J. Atmos. Sci.* **31**: 543–550.

Bennett AJ, Harrison RG. 2009. Evidence for global circuit current flow through water droplet layers. *J. Atmos. Solar-Terr. Phys.* **17**: 1219–1221, doi: 10.1016/j.jastp.2009.04.011.

Bott A. 2000. A flux method for the numerical solution of the stochastic collection equation: Extension to two-dimensional particle distributions. *J. Atmos. Sci.* **57**: 284–294, doi: 10.1175/1520-0469(2000)057<0284: AFMFTN>2.0.CO;2.

Chalmers JA. 1967. *Atmospheric Electricity* (2nd edn). Pergamon Press: Oxford, UK.

Davis MH. 1964. Two charged spherical conductors in a uniform electric field: Forces and field strength. *Q. J. Mech. Appl. Math.* **17**: 499–511.

Fletcher NH. 2014. Reply to Comments on 'Effects of charge on collisions between cloud droplets'. *J. Appl. Meteorol. Clim.* **53**: 1321.

Gunn R. 1954. Diffusion charging of atmospheric droplets by ions and the resulting combination coefficients. *J. Meteorol.* **11**: 339–347.

Harrison RG. 2012. Aerosol-induced correlation between visibility and atmospheric electricity. *J. Aerosol Sci.* **52**: 121–126.

Harrison RG. 2013. The Carnegie curve. *Surv. Geophys.* **34**: 209–232, doi: 10.1007/s10712-012-9210-2.

Harrison RG. 2015. *Meteorological Measurements and Instrumentation*. Wiley-Blackwell: Chichester, UK.

Harrison RG, Ambaum MHP. 2008. Enhancement of cloud formation by droplet charging. *Proc. R. Soc. London A* **464**: 2561−2573.

Harrison RG, Ambaum MHP. 2013. Electrical signature in polar night cloud base variations. *Environ. Res. Lett.* **8**: 015027, doi: 10.1088/1748-9326/8/1/015027.

Harrison RG, Carslaw KS. 2003. Ion−aerosol−cloud processes in the lower atmosphere. *Rev. Geophys.* **41**: 1012, doi: 10.1029/2002RG000114.

Harrison RG, Nicoll KA. 2014. Note: Active optical detection of cloud from a balloon platform. *Rev. Sci. Instrum.* **85**: 066104, doi: 10.1063/1.4882318.

Harrison RG, Usoskin I. 2010. Solar modulation in surface atmospheric electricity. *J. Atmos. Solar-Terr. Phys.* **72**: 176−182.

Harrison RG, Joshi M, Pascoe K. 2011. Inferring convective responses to El Niño with atmospheric electricity measurements at Shetland. *Environ. Res. Lett.* **6**: 044028, doi: 10.1088/1748-9326/6/4/044028.

Harrison RG, Nicoll KA, Lomas AG. 2012. Programmable data acquisition system for research measurements from meteorological radiosondes. *Rev. Sci. Instrum.* **83**: 036106, doi: 10.1063/1.3697717.

Harrison RG, Nicoll KA, Aplin KL. 2014. Vertical profile measurements of lower troposphere ionisation. *J. Atmos. Solar-Terr. Phys.* **119**: 203−210, doi: 10.1016/j.jastp.2014.08.006.

Khain A, Arkhipov V, Pinsky M, Feldman Y, Ryabov Y. 2004. Rain enhancement and fog elimination by seeding with charged droplets. Part I: Theory and numerical simulations. *J. Appl. Meteorol.* **43**: 1513−1529.

Klimin NN, Rivkind VY, Pachin VA. 1994. Collision efficiency calculation model as a software tool for microphysics of electrified clouds. *Meteorol. Atmos. Phys.* **53**: 111−120.

Lekner J. 2012. Electrostatics of two charged conducting spheres. *Proc. R. Soc. London A* **471**: 2174, doi: 10.1098/rspa.2012.0133.

Mach DM, Blakeslee RJ, Bateman MG. 2011. Global electric circuit implications of combined aircraft storm electric current measurements and satellite-based diurnal lightning statistics. *J. Geophys. Res.* **116**: D05201, doi: 10.1029/2010JD014462.

Marsh ND, Svensmark H. 2000. Low cloud properties influenced by cosmic rays. *Phys. Rev. Lett.* **85**: 5004−5007.

Mason BJ. 1971. *The Physics of Clouds* (2nd edn). Clarendon Press: Oxford, UK.

Miles NL, Verlinde J, Clothiaux EE. 2000. Cloud droplet size distributions in low-level stratiform clouds. *J. Atmos. Sci.* **57**: 295−311.

Neff U, Burns SJ, Mangini A, Mudelsee M, Fleitmann D, Matter A. 2001. Strong coherence between solar variability and the monsoon in Oman between 9 and 6 kyr ago. *Nature* **411**: 290−293, doi: 10.1038/35077048.

Nicoll KA. 2012. Measurements of atmospheric electricity aloft. *Surv. Geophys.* **33**: 991−1057.

Nicoll KA. 2013. Note: A self-calibrating electrometer for atmospheric charge measurements from a balloon platform. *Rev. Sci. Instrum.* **84**: 096107, doi: 10.1063/1.4821500.

Nicoll KA, Harrison RG. 2009. Vertical current flow through extensive layer clouds. *J. Atmos. Solar-Terr. Phys.* **71**: 2040−2046.

Nicoll KA, Harrison RG. 2012. Balloon-borne disposable radiometer for cloud detection. *Rev. Sci. Instrum.* **83**: 025111, doi: 10.1063/1.3685252.

Nicoll KA, Harrison RG. 2014. Detection of lower tropospheric responses to solar energetic particles at midlatitudes. *Phys. Rev. Lett.* **112**: 225001, doi: 10.1103/PhysRevLett.112.225001.

Pruppacher HR, Klett JD. 1998. *Microphysics of Cloud and Precipitation* (2nd edn). Kluwer Academic Publishers: Dordrecht, Netherlands.

Russell A. 1922. The problem of two electrified spheres. *Proc. Phys. Soc. London* **35**: 10−29.

Rycroft MJ, Israelsson S, Price C. 2000. The global atmospheric electric circuit, solar activity and climate change. *J. Atmos. Solar-Terr. Phys.* **62**: 1563−1576.

Rycroft MJ, Nicoll KA, Aplin KL, Harrison RG. 2012. Recent advances in global electric circuit coupling between the space environment and the troposphere. *J. Atmos. Solar-Terr. Phys.* **90-91**: 198−211.

Sátori G, Zieger B. 1999. El Niňo related meridional oscillation of global lightning activity. *Geophys. Res. Lett.* **26**: 1365−1368, doi: 10.1029/1999GL900264.

Schlamp RJ, Pruppacher HR, Hamielec AE. 1975. A numerical investigation of the efficiency with which simple columnar ice crystals collide with supercooled water drops. *J. Atmos. Sci.* **32**: 2330−2337.

Smythe WR. 1950. *Static and Dynamic Electricity* (2nd edn). McGraw-Hill: New York, NY.

Takahashi Y, Okazaki Y, Sato M, Miyahara H, Sakanoi K, Hong PK, Hoshino N. 2010. 27-day variation in cloud amount in the western Pacific warm pool region and relationship to the solar cycle. *Atmos. Chem. Phys.* **10**: 1577−1584, doi: 10.5194/acp-10-1577-2010.

Thomson W. 1853. On the mutual attraction or repulsion between two electrified spherical conductors. In *Reprint of Papers on Electrostatics and Magnetism*. Macmillan: London, 86−97.

Tinsley BA. 2000. Influence of solar wind on the global electric circuit, and inferred effects on cloud microphysics, temperature and dynamics in the troposphere. *Space Sci. Rev.* **94**: 231−258.

Tinsley BA, Zhou L. 2014. Comments on 'Effects of charge on collisions between cloud droplets'. *J. Appl. Meteorol. Clim.* **53**: 1317−1320.

Tinsley BA, Rohrbaugh RP, Hei M, Beard KV. 2000. Effects of image charges on the scavenging of aerosol particles by cloud droplets and on droplet charging and possible ice nucleation processes. *J. Atmos. Sci.* **57**: 2118−2134.

Tripathi SN, Harrison RG. 2002. Enhancement of contact nucleation by scavenging of charged aerosol particles. *Atmos. Res.* **62**: 57−70.

Whipple FJW, Scrase FJ. 1936. Point discharge in the electric field of the Earth. *Geophys. Mem. Meteorol. Off. London* **7**: 1−68, M. O. 356k.

Wilson CTR. 1921. Investigations on lightning discharges and the electric field of thunderstorms. *Philos. Trans. R. Soc. London A* **221**: 73−115.

Wilson CTR. 1929. Some thundercloud problems. *J. Franklin Inst.* **208**: 1−12.

Zhou L, Tinsley BA. 2007. Production of space charge at the boundaries of layer clouds. *J. Geophys. Res.* **112**: D11203, doi: 10.1029/2006JD007998.